# Marrying Materials and Processes: A Superstructure Inspired Optimization Approach For Pressure Swing Adsorption Based Carbon Dioxide Capture Processes

Amir Mohammad Elahi,[†] Sayed Alireza Hosseinzadeh Hejazi,[*,†,‡] and Ashwin Kumar Rajagopalan[*,¶]

[†]*Department of Chemical Engineering, Amirkabir University of Technology (Tehran Polytechnic), Tehran, 159163-4311, Iran*

[‡]*Office of Sustainability, Amirkabir University of Technology (Tehran Polytechnic), Tehran, 159163-4311, Iran*

[¶]*Department of Chemical Engineering, The University of Manchester, Manchester, M13 9PL, United Kingdom*

E-mail: a.hejazi@aut.ac.ir; ashwinkumar.rajagopalan@manchester.ac.uk

**Abstract**

The performance of an adsorption-based separation process is dictated by the choices of the solid sorbent and the process configuration. Often screening of materials and process configuration is performed using digital twins that mimic a real adsorption process. In typical studies, either several materials are screened for a specific process configuration to find the best candidate or the performance of several process configurations is evaluated for a specific material. However, it has long been suggested

that to truly maximize the potential of a given material, it should be "married" to processes. In this work, we address the "marriage" of materials and processes through three dedicated goals. First, to develop a modeling framework for an all-encompassing pressure swing adsorption cycle composed of several process configurations. Second, to develop an optimization framework, drawing inspiration from superstructures, to select the optimal process configuration from the all-encompassing cycle to reach a given process target. Third, to highlight the importance and relevance of such an approach that enables each material to truly maximize its potential, by varying both the process configuration and the corresponding operating conditions. To address these goals, we have developed a computational framework composed of a process model and a process optimizer. Subsequently, using this computational framework, we have evaluated the performance of several real and hypothetical materials. Our computational studies led to two key outcomes, namely, (1) to employ an integrated material-process optimization approach to maximize the true potential of any material when screening for a given application and when evaluating the performance under different feed conditions; and (2) not to generalize the observations regarding the best process configuration from one material to every other material.

# 1 Introduction

Gas separation and purification are widely used for many industrially important applications such as $O_2/N_2$, $He/CH_4$, diene/olefin, and $N_2/CH_4$ separation, to name a few.[1–4] To this aim, one of the well-established technologies used is adsorption-based separation processes, in which a solid sorbent is used to selectively adsorb a target gas while rejecting the others.[5,6] Two key design factors dictate the performance of any adsorption-based separation process, namely, the solid material, i.e., the adsorbent, and the process configuration, a.k.a the cycle. From the materials point of view, a plethora of organic and inorganic materials have been developed over the years to perform gas separation and purification.[7,8] In recent years,

computational material discovery, advances in material synthesis (in the form of reticular chemistry), and material characterization have led to an exponential growth of new materials being reported for different applications.[9,10] From the process point of view, adsorption-based separation can be carried out in several different ways based on the technique used for the regeneration of the solid adsorbent. They can broadly be categorized into pressure swing adsorption, vacuum swing adsorption, temperature swing adsorption, concentration swing adsorption, electric swing adsorption processes, or a combination of these. Depending on the type, several process configurations can be envisioned that might tackle achieving high purity and high recovery for a target gas, or a low energy consumption for a given process. Given the substantial number of materials that are discovered and the potential growth in this field in the future, choosing the right material and the right process configuration for a given separation problem will gain more significance in the coming years.[8]

It is well-known that choosing the right material and the process is crucial to have an efficient separation process. There are several metrics, for instance, selectivity, working capacity, and equilibrium loading, which have been used over the years to rank materials.[11,12] Alas, even though these metrics are easy to compute, due to their simple algebraic formulation, it is widely accepted that these simple metrics cannot capture the complexities of a process. Therefore, they are unable to accurately rank adsorbents based on their process performance.[8,13–15] To overcome this, process-based screening of materials using mathematical models is essential. Two classes of process models exist in the literature, namely, simplified models[16–20] and detailed models.[13,21–25] The difference between these models typically arises from their ability to describe mass, heat, and momentum transfer along the spatial coordinate of an adsorption column (detailed models) or not (simplified models). Given the two design factors involved in the adsorption processes, one can perform such screening by either fixing a process configuration and evaluating the performance of several materials from a database or by selecting a material and assessing its performance in several process configurations. Most material screening studies use the former approach, thereby discarding cycles

that might offer great potential for previously unexplored materials. The latter approach has often been applied only to understand the behavior of a single or at best a few materials under different process settings and it has not been employed for large-scale material screening studies. When undertaking a process-based screening study using detailed models, one aims to explore a range of operating conditions to ensure that the adsorbent gets to maximize its potential within the bounds of the processes. Albeit, this comes with a disadvantage, i.e., they are time-consuming. This is attributed to the computational cost involved in solving adsorption process models, composed of coupled nonlinear partial differential equations (PDEs) to describe mass, momentum, and heat transfer. An additional layer of complexity and computational cost is added when a process optimizer is wrapped around these models to explore different operating conditions.[26] This makes the overall process of adsorbent and process screening tedious. Recently, some – if not all – of these challenges have been addressed by developing machine learning models for specific separation problems and process configurations.[27] A less explored, but a promising technique, to perform an integrated material and process configuration screening is to employ a superstructure-based optimization approach. Here, a superstructure corresponds to an all-encompassing process configuration that is a superset of all possible process configurations. In this approach, the superstructure is optimized as a whole, instead of optimizing individual process configurations, thereby leading to computational time benefits. This has been previously employed within the context of synthesizing optimal pressure swing adsorption (PSA) cycles for precombustion $CO_2$ capture and finding optimal operating strategies for simulated moving bed chromatography schemes.[28–30]

In our work, we aim to tap into the unexplored potential that a superstructure-based optimization approach offers for performing an integrated material-process configuration screening for adsorptive gas separation. To this aim, we provide the motivation and the problem statement for this work in Section 2. This is followed by the choice of separation problem, materials and process configurations in Section 3. In Section 4, we describe the

computational framework, i.e., process modeling and process optimization tools developed in this work to perform the integrated optimization. We provide the results obtained by performing several case studies to highlight the relevance of performing an integrated optimization using a superstructure in Section 5. Finally, we conclude by providing a summary of key outcomes, key limitations, and the way forward in Section 6.

# 2 Problem Statement

Despite the cumbersome methodology involved in process-based screening, it has long been suggested that to truly maximize the performance of any given adsorbent, they should be "married" to process(es).[4,31,32] This approach has the potential to capture scenarios in which the best process configuration for a given material is not a single process configuration. In more detail, depending on the process requirements, a material might make use of different process configurations to reach its target, thereby truly maximizing its potential. Additionally, this approach can also capture scenarios in which the best process configuration varies among different materials. Despite the implication of such outcomes, studies that aim to systematically develop and validate methodologies to "marry" adsorbents and processes have not been undertaken due to technical challenges from modeling and optimizing the combined material-process system.

The overarching goal of this study is threefold. First, to develop a robust modeling framework that enables the "marriage" of any given adsorbent with process(es). Second, to develop an optimization framework to simultaneously screen multiple process configurations using a single optimization run for a material with the aforementioned modeling framework. Finally, and most importantly, to highlight the importance of incorporating such a modeling and optimization framework to screen several materials that enables *truly* exploiting the best out of each material. We have developed our methodology drawing inspiration from previously reported studies employing a superstructure-based optimization of adsorp-

tion and chromatography processes.[28–30] A conceptual schematic of the problem and the expected outcome is illustrated in Figure 1. The core of the computational framework is the process, referred to as the *Superstructure*, and it is composed of two process configurations in this figure, namely, *Configuration A* (red) and *Configuration B* (green). Traditionally, these two process configurations will be optimized independently, to maximize/minimize key performance indicators for the *Material*, leading to a cloud of data points corresponding to a given performance(s) obtained at a specified set of operating conditions, as shown on the performance panel (green markers for Configuration A and red markers for Configuration B). In the approach to be presented in the subsequent sections, instead of independently optimizing the configurations, we will optimize the *superstructure* (blue markers) composed of a given number of configurations (in Figure 1, two configurations). We will incorporate the choice of the process configuration as an operating variable and the optimizer determines the best process configuration to reach a given performance(s). Ideally, the best performance(s) estimated by the *superstructure* should match the best performances estimated by the independent evaluation of the constituent process configurations (red and green markers in the performance panel of Figure 1). Note that we follow a slightly modified definition of the superstructure in this work. Traditionally, for our problem, a true superstructure translates to a superset of all possible process configurations.[33] However, in our work, the *superstructure* refers to a small subset of them. To address the aforementioned goals of the study, we have identified two sub-tasks, namely, (a) create a modeling framework to simulate a *superstructure* (see Section 4.1) and (b) identify and validate an optimization routine to optimize the *superstructure* (see Section 4.2). We have considered a specific separation problem as a toy example (see Section 3), to develop the aforementioned computational framework and to systematically highlight the relevance of this work.

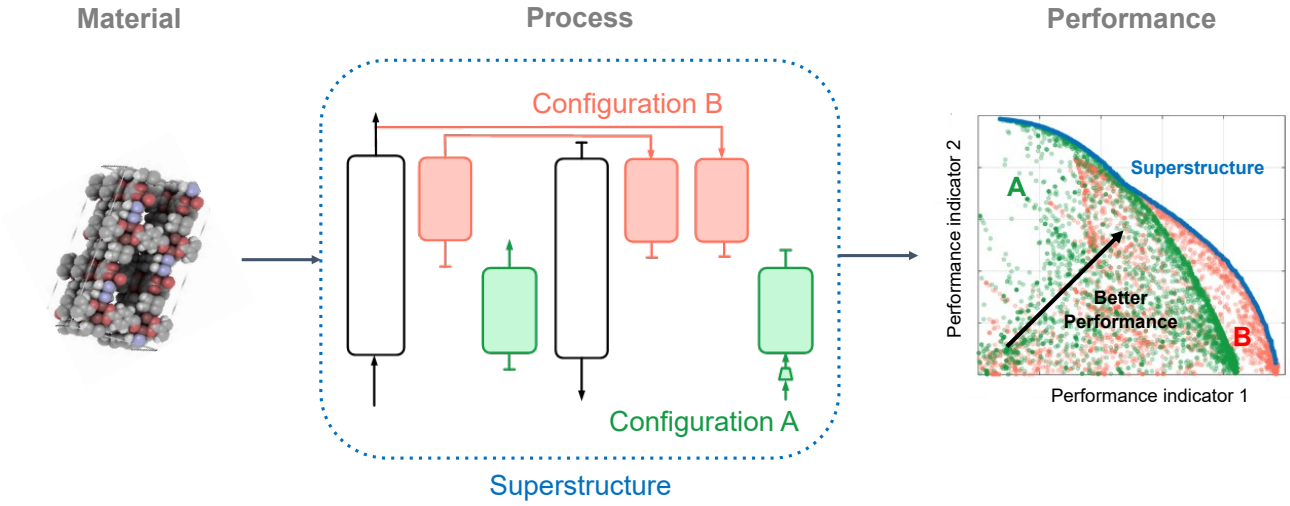


Figure 1: A visual schematic of the proposed *superstructure* optimization framework. The "Material" [34] is optimized using a *superstructure* (dotted blue box in the "Process" panel) composed of two process configurations, A and B. The columns highlighted in green and red correspond to the process steps integral to configurations A and B, respectively, while the columns highlighted in black corresponds to the process steps that exist in both the process configurations. The material-*superstructure* combination is optimized to maximize two performance indicators (1 and 2 in the "Performance" panel). The green and red markers correspond to the performances evaluated independently using configurations A and B, respectively, and the blue markers correspond to the performances evaluated using the superstructure. Note that ideally, the performances of the combined process configurations (A and B) should match with the one of the superstructure.

# 3 Case Study

## 3.1 Separation Problem

In this work, we consider precombustion $CO_2$ capture as the separation problem of interest. In this process, we aim to separate $CO_2$ from $H_2$ in a syngas stream produced in hydrogen production units.[35] We assume the feed stream to be a binary mixture of $CO_2$ (40 %) and $H_2$ (60 %) available at 34.5 bar and 240 °C. We perform this separation using a PSA process with solid adsorbents (see Section 3.2). Using the knowledge from a prior study,[36] we have considered three different process configurations (see Section 3.3) to perform the aforementioned separation.

## 3.2 Choice of Materials

To highlight the importance of incorporating a *superstructure*-based modeling and optimization framework, we have tested the performance of several materials, both real and hypothetical. We assume a previously reported and experimentally tested material, TDA AMS-19 (an activated carbon)[36,37] as the reference material (referred to as REF in the subsequent sections). The equilibrium adsorption capacity in this material is described using a Sips isotherm model. Subsequently, we generate isotherms for several hypothetical materials by varying the isotherm model parameters of the reference material for both $CO_2$ and $H_2$,[36] thereby varying the shape of the isotherm and the adsorption capacity at a given condition. We assume that the extended Sips isotherm model describes the competitive adsorption on the materials considered in this work. The equilibrium solid phase concentration $q_i^*(p_i, T)$ $[\mathrm{mol\,kg^{-1}}]$ of component $i$ at a given partial pressure $p_i$ [Pa] and temperature $T$ [K] is given by the Sips isotherm model as

$$q_i^* = \frac{q_{i,\mathrm{sat}}(k_i p_i)^{s_i}}{1 + \sum_{i=1}^{n}(k_i p_i)^{s_i}} \tag{1}$$

where $n$ is the number of gases, $q_{i,\mathrm{sat}}$ $[\mathrm{mol\,kg^{-1}}]$ is the saturation capacity of the adsorbent, $s_i$ [–] is the adsorption model parameter, and $k_i$ $[\mathrm{Pa^{-1}}]$ is the adsorption equilibrium constant of component $i$. The latter three parameters are temperature dependent and are described as

$$\begin{aligned} q_{i,\mathrm{sat}} &= \omega_i \mathrm{e}^{-\frac{\varphi_i}{\mathrm{R}T}} \\ k_i &= \theta_i \mathrm{e}^{-\frac{\phi_i}{\mathrm{R}T}} \\ s_i &= s_{1,i} \arctan\left(s_{2,i}(T - T_{\mathrm{ref}})\right) + s_{\mathrm{ref},i} \end{aligned} \tag{2}$$

where $\omega_i$ $[\mathrm{mol\,kg^{-1}}]$, $\varphi_i$ $[\mathrm{J\,mol^{-1}}]$, $\theta_i$ $[\mathrm{Pa^{-1}}]$, $\phi_i$ $[\mathrm{J\,mol^{-1}}]$, $s_{1,i}$ [–], $s_{2,i}$ [–], $T_{\mathrm{ref}}$ [K] and

$s_{i,\text{ref}}$ [–] are the Sips isotherm fitting parameters. To generate the isotherms of the different hypothetical materials, we vary four parameters, i.e., $\omega_i$, $s_{i,1}$, $s_{i,2}$, and $s_{i,\text{ref}}$. We vary these parameters to obtain materials that fall under three categories, namely, materials with the (i) same $H_2$ isotherm as the reference material but with different nonlinearity and capacity of $CO_2$ isotherms; (ii) same $CO_2$ isotherm as the reference material but with different nonlinearity and capacity of $H_2$ isotherms; and (iii) different nonlinearity and capacity for both $CO_2$ and $H_2$ isotherms when compared to the reference material. The isotherms of the reference material (REF, dark curve) and the other hypothetical materials (light curves) at 240 °C for $CO_2$ (panel(a)) and $H_2$ (panel(b)) are illustrated in Figure 2. The corresponding isotherm parameters of both the reference and the hypothetical materials for both $CO_2$ and $H_2$ are provided in Section S1 in the Supporting Information.

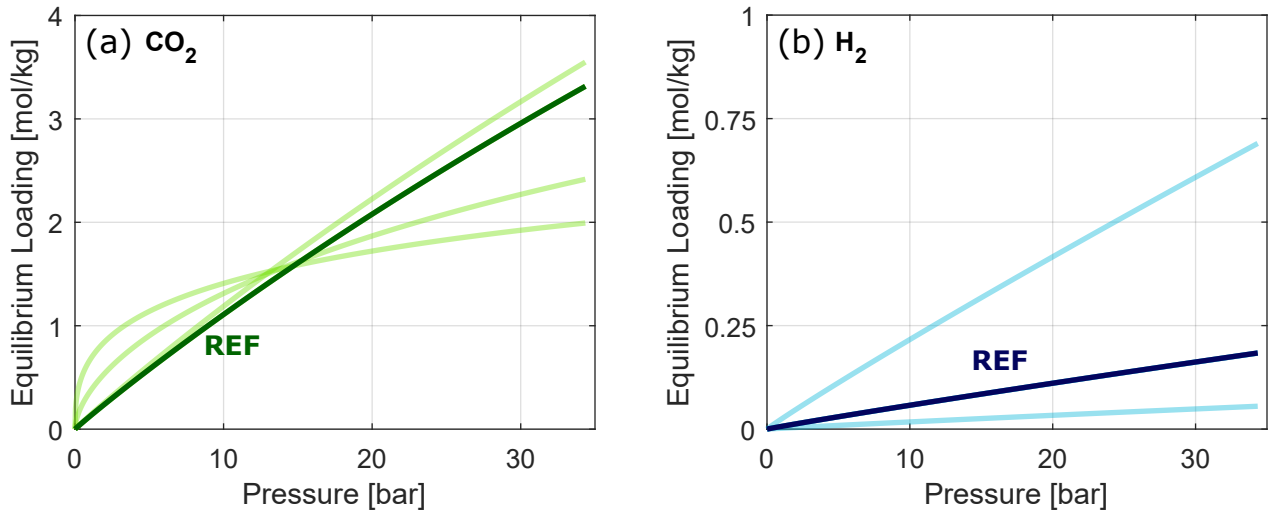


Figure 2: Adsorption equilibrium loading obtained using the single component Sips isotherm, given by eq 1, for **(a)** $CO_2$ and **(b)** $H_2$ at 240 °C for the reference material (REF, TDA AMS-19) and the hypothetical materials. The darker shade of the curves corresponds to the reference material and the lighter shade of the curves corresponds to all the hypothetical materials used in this work.

## 3.3 Choice of Process Configurations

We construct a *superstructure* composed of three process configurations. These configurations are: (1) basic 4-step cycle; (2) 5-step cycle with pressure equalization (PE) and light product pressurization (LPP); and (3) 4-step cycle with LPP. The *superstructure* considered in this work along with its constituent process configurations is visualized in Figure 3 (see also Section S2 in the Supporting Information). The steps visualized in violet, red and green colors, correspond to the basic 4-step cycle, 4-step cycle with LPP, and 5-step cycle with PE and LPP, respectively. The steps visualized in black color are common for all the three process configurations. All the three cycles were studied in detail in a previously reported work and have their advantages and disadvantages in terms of reaching certain process performance targets.[36]

The process configurations in the *superstructure* are composed of six basic steps. One can generate more than three process configurations with these six steps. However, for the sake of clarity and to conclusively highlight the relevance of the approach presented in this work, we have restricted ourselves to the aforementioned three process configurations. Further, for the discussions presented in Sections 5.1 through 5.3.1, we have used only two configurations, namely, the basic 4-step cycle and the 5-step cycle with PE and LPP. The six steps in the *superstructure* are adsorption (ADS), co-current blowdown (CoBLO), counter-current blowdown (CnBLO), feed pressurization (FP), pressure equalization (PE), and light product pressurization (LPP). We perform these steps in a packed bed column of length $L$ filled with the solid sorbent. In the ADS step, we introduce the binary feed at $z = 0$ to the column at a high pressure $P_{\mathrm{H}} = 34.5\,\mathrm{bar}$, a feed temperature $T = 240\,^{\circ}\mathrm{C}$, and a $CO_2$ mole fraction $y_{\mathrm{f,CO_2}} = 0.40$. In this step, we saturate the adsorbent with the heavy component ($CO_2$) and we obtain a stream rich in the light component ($H_2$) at $z = L$. In the CoBLO step, we close the $z = 0$ end of the column to remove – primarily – the light product from $z = L$ end of the column by reducing the pressure from $P_{\mathrm{H}}$ to an intermediate pressure $P_{\mathrm{INT}}$. If we replace the CoBLO step with a PE step, we transfer the gas obtained from the $z = L$

end of the column (referred to as the donor column, PED) at a high pressure $P_{\mathrm{H}}$ to another column (referred to as the receiver column, PER) at a low pressure $P_{\mathrm{L}}$. This step leads to the pressure in the donor and the receiver columns to be equalized at the intermediate pressure $P_{\mathrm{INT}}$. This step plays a favorable role in increasing the heavy product recovery and lowering the overall energy consumption of the process.[38] Note that for a standard CoBLO step, we can vary $P_{\mathrm{INT}}$ arbitrarily, but for the PE steps, because of the underlying physics, $P_{\mathrm{INT}}$ cannot be varied. Using an approach presented in an earlier work, we compute the $P_{\mathrm{INT}}$ as a function of $P_{\mathrm{H}}$ and $P_{\mathrm{L}}$. We obtain a new functional form for each material considered in this work as it depends on the isotherm of the material studied.[38] In the CnBLO step, we close the $z = L$ end of the column to remove – primarily – the heavy product from $z = 0$ end of the column by reducing the pressure from $P_{\mathrm{INT}}$ to $P_{\mathrm{L}}$. In the FP step, we introduce the binary feed at $z = 0$ (with the $z = L$ end closed) to the column at a high pressure $P_{\mathrm{H}} = 34.5\,\mathrm{bar}$, a feed temperature $T = 240\,^{\circ}\mathrm{C}$ and a $CO_2$ mole fraction $y_{\mathrm{f,CO_2}} = 0.40$. In this step, we increase the pressure from the lower pressure at the preceding step to $P_{\mathrm{H}}$ to bring back the column to its initial state to take in fresh feed for the separation. Finally, in the LPP step, instead of using the feed gas (as in the case of FP), we use the light product obtained in the ADS step to pressurize the column back to its initial state. This step plays a favorable role in increasing the purity of the heavy product. Note that if there is an insufficient quantity of gas from the ADS step to pressurize the column, we supplement this step with the FP step. Depending on the process configuration, we execute these steps in a cyclic fashion until the process reaches a cyclic steady state (CSS). We assume this condition to be met in our model when the overall mass balance error over five consecutive cycles of the process is below 1 %.

All the three process configurations, shown in Figure 3, share two steps in common, namely, ADS and CnBLO. The basic 4-step cycle and the 4-step cycle with LPP share the CoBLO step. Finally, the 4-step cycle with LPP and the 5-step cycle with the PE and LPP share the LPP step. In the implementation of the *superstructure*, we have a single cycle that incorporates all the six steps. To switch between the different configurations, we turn off the

steps that are not part of the specific configuration being explored. In more detail, to use the basic 4-step cycle, we turn off the PED, PER, and LPP steps. To use the 4-step cycle with LPP, we turn off the PED, PER, and FP steps. Finally, to use the 5-step cycle with PE and LPP, we turn off the CoBLO and FP steps. To summarize, the constituent process configurations and the order of the steps are as follows:

1. *Basic 4-step cycle*: ADS - CoBLO - CnBLO - FP

2. *5-step cycle with PE and LPP*: ADS - PED - CnBLO - PER - LPP - (FP)

3. *4-step cycle with LPP*: ADS - CoBLO - CnBLO - LPP - (FP)

As mentioned previously, the FP in the last two configurations is used only if the LPP step is unable to bring back the column to its initial state.

# 4 Process Modeling and Optimization

## 4.1 Process Modeling

In this work, we use a detailed one-dimensional axially dispersed plug flow model described elsewhere,[39] to simulate the six steps described in Section 3.3. Based on the boundary conditions, we can group these steps into three categories, i.e., open-open (ADS), open-closed (CnBLO, PED, and FP), and closed-open (CoBLO and PER). For these three categories, using the given initial and boundary conditions, we write the corresponding mass, momentum, and heat transfer balances to model the steps and in turn the entire process configuration. We build the model by making several assumptions. First, we assume an ideal gas phase and an instantaneous thermal equilibrium between the solid and the gas phase. Second, we assume the mass transfer between the solid and the gas phase to be defined by the linear driving force model and the mass transfer resistance to exist only in the macropores of the functionalized adsorbent. Third, we use Darcy's law to describe the pressure drop in the

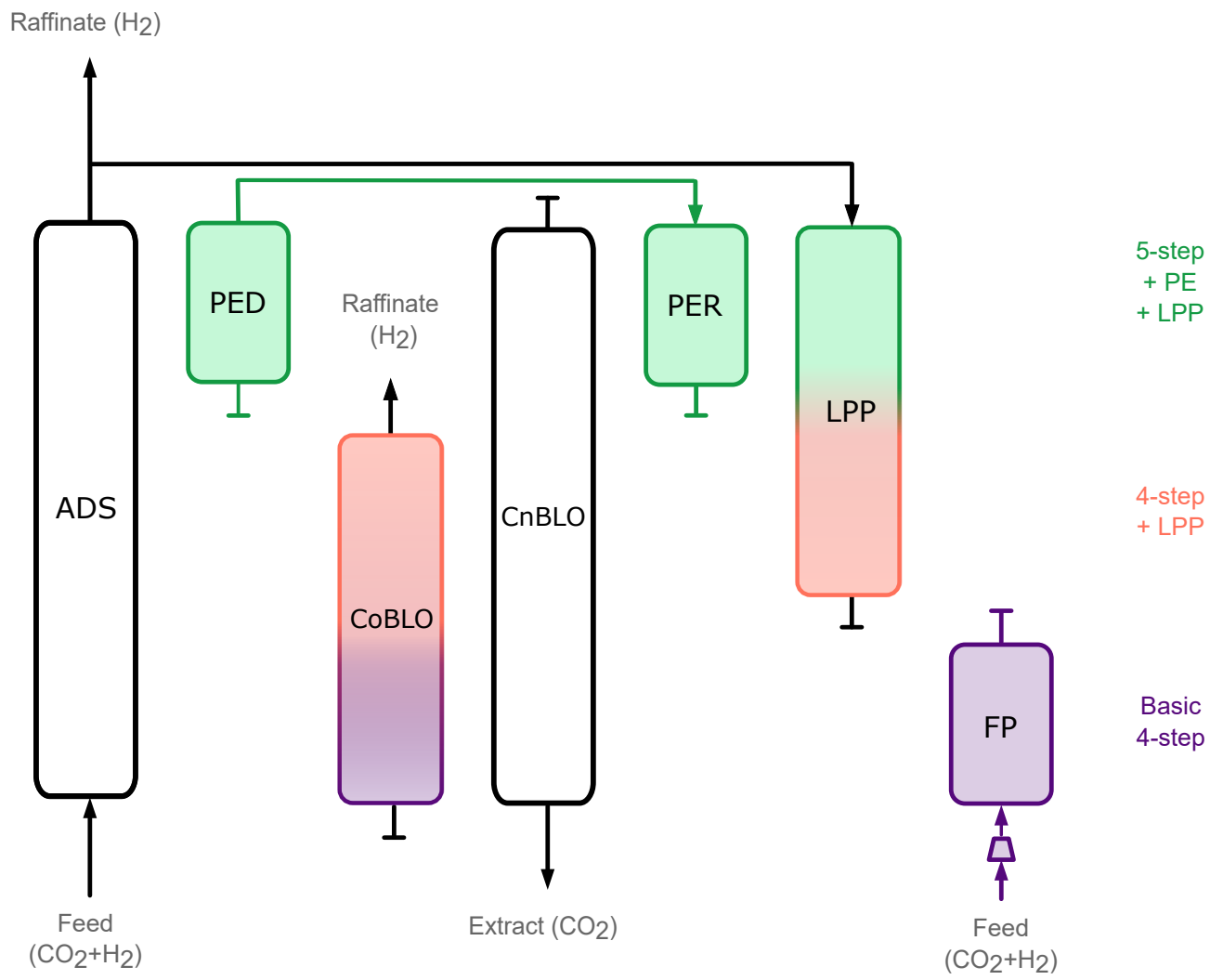


Figure 3: Schematic of the *Superstructure* considered in this study. The *superstructure* is composed of three process configurations, namely, the basic 4-step cycle (violet), the 4-step cycle with LPP (coral), and the 5-step cycle with PE and LPP (green). The steps in the process are adsorption (ADS), co-current blowdown (CoBLO), counter-current blowdown (CnBLO), feed pressurization (FP), pressure equation donor (PED) and receiver (PER), and light product pressurization (LPP). The columns highlighted in black correspond to the process steps that exist in all the three configurations. The columns highlighted in two colors (violet/coral and coral/green) corresponds to the process steps that exist in the corresponding two configurations. Depending on the process configuration, the feed to the process is introduced either in the FP and the ADS step or in the ADS step. Depending on the process configuration, the raffinate/light product ($H_2$) is collected either in the ADS step or in the ADS and CoBLO step. For all the process configurations, the extract/heavy product ($CO_2$) is collected in the CnBLO step. The individual process configurations and the corresponding pressure profiles in each of the process step are provided in Section S2 in the Supporting Information.

column along its axial direction. Fourth, we assume that the adsorbent physical properties, bed porosity, density, and viscosity of the gas phase are uniform throughout the column. We solve the resulting system of coupled partial differential equations (PDEs) in two steps. First, we discretize them in space using a finite volume method with a van-Leer flux limiter.[40] Second, we integrate the resulting system of ordinary differential equations (ODE) over the time span of a given step using a stiff ODE solver `ode23s` available in MATLAB R2020a. The system of PDEs along with the corresponding initial and boundary conditions are provided in Sections S3 and S4 in the Supporting Information. The simulation parameters used in the model are provided in Section S5 in the Supporting Information. We performed all the simulations in the Computational Shared Facility at the University of Manchester using a CPU node composed of $2 \times 16$-core Intel Xeon Gold 6130 CPU @ 2.10GHz with 192GB RAM. Note that this model has been extensively validated in experimental settings in both lab- and pilot-scale for different separation problems.[41–45]

## 4.2 Process Optimization

Over the years, adsorption separation processes have been optimized to maximize or minimize one or more process performance indicators. These indicators include purity, recovery, energy consumption, productivity, to name a few.[38,46] Depending on the formulation of the optimization routine, they can be classified either as a single- or a multiobjective problem. For the former class of problems, within the context of adsorption processes, the goal would be to either maximize/minimize a single performance indicator or to maximize/minimize a collective quantity that condenses multiple performance indicators into one. For the latter class of problems, within the context of adsorption processes, the goal would be to maximize/minimize multiple performance indicators simultaneously. Different values of performance indicators are accessed by the optimizer by varying the operating conditions of the process (referred to as the decision variables), namely, the pressures, the step times, the feed velocity, to name a few. Irrespective of the class of problem, optimizing adsorption processes

require employing derivative-free optimization methods due to the nonlinear and nonconvex nature of the objectives and the constraints, if any, imposed on the process.[39,47]

In this work, we employ two different derivative-free optimization methods with single and multiple objectives to optimize the process configurations. We use a single objective optimization method to optimize the *superstructure*, presented in Section 3.3 (see Section 4.2.2). To validate the optimal performance obtained from the *superstructure*, we perform independent multiobjective optimization runs for the constituent process configurations (see Section 4.2.1). The reason for undertaking these two different approaches and the challenges associated with them is elaborated in the discussion provided in the following sections.

For all the optimization results presented in this work, we target two performance indicators, namely, the purity $Pu_{\mathrm{CO_2}}$ [%] and recovery $Re_{\mathrm{CO_2}}$ [%] of the heavy product ($CO_2$), which is obtained in the extract stream. These two indicators are defined as

$$Pu_{\mathrm{CO_2}} = \frac{n^{\mathrm{EXT}}_{\mathrm{CO_2}}}{n^{\mathrm{EXT}}_{\mathrm{CO_2+H_2}}} \tag{3}$$

$$Re_{\mathrm{CO_2}} = \frac{n^{\mathrm{EXT}}_{\mathrm{CO_2}}}{n^{\mathrm{F}}_{\mathrm{CO_2}}} \tag{4}$$

where $n_i$ [mol] is the number of moles of gas $i$ either in the extract (EXT) or in the feed (F) stream, which is obtained by solving the complete process model described in Section 4.1. Note that for all the process configurations, the extract stream corresponds to the outlet from the CnBLO step and depending on whether the FP step is used or not, the feed corresponds to the inlet streams to the FP and the ADS or the ADS step, respectively.

### 4.2.1 Single Cycle Optimization

In most of the multiobjective optimization studies reported for PSA processes, specifically maximization of purity and recovery, the optimization problem is framed to minimize the following two objectives $J_1$ [–] and $J_2$ [–]

$$J_1 = \frac{1}{\left(Pu_{\mathrm{CO_2}}/100\right)}$$
$$J_2 = \frac{1}{\left(Re_{\mathrm{CO_2}}/100\right)} \tag{5}$$

where $Pu_{\mathrm{CO_2}}$ and $Re_{\mathrm{CO_2}}$ can be obtained from eqs 3 and 4, respectively. This approach has been typically employed either to optimize a given process configuration for a given material or to evaluate the optimal performances of several process configurations – independently – for a given material. In this work, we have used this multiobjective approach to validate the outcome from the *superstructure* optimization, discussed in Section 4.2.2. To this end, we evaluate the performance of all the three process configurations, discussed in Section 3.3, independently for the reference material. We optimize these process configurations by exploring the corresponding operating conditions (decision variables). For the basic 4-step cycle and the 4-step cycle with LPP, the decision variables (DVs) are the step times of ADS ($t_{\mathrm{ADS}}$), CoBLO ($t_{\mathrm{CoBLO}}$) and CnBLO ($t_{\mathrm{CnBLO}}$), the intermediate pressure ($P_{\mathrm{INT}}$) and low pressure ($P_{\mathrm{L}}$), and the feed velocity ($v_{\mathrm{f}}$). For the 5-step cycle with PE and LPP, the DVs are all of the aforementioned variables except the intermediate pressure ($P_{\mathrm{INT}}$), due to reasons explained in Section 3.3. The bounds for these DVs are provided in Section S6 in the Supporting Information. Note that all the variables are continuous in nature, therefore, this is a nonlinear programming (NLP) problem, i.e., the objective of the problem is nonlinear with continuous variables. To perform the aforementioned process optimization, we have used a multiobjective derivative-free optimizer (`paretosearch` in MATLAB R2020a) based on a pattern search algorithm. In a typical pattern search iteration, the optimizer either explores a new set of decision variables that aims to minimize the objective function or shrinks the size of the step for the next iteration to move toward a minimum if no set of decision variables is better than the current one. At the end of the optimization run, we obtain three independent Pareto fronts that describe the trade-off between purity and recovery for the cor-

responding three configurations. The Pareto fronts shown in the subsequent sections denotes the best possible performance that the material-process combination can achieve in terms of $CO_2$ purity and recovery. The optimizer parameters for the `paretosearch` algorithm are provided in Section S7 in the Supporting Information.

### 4.2.2 *Superstructure* Optimization

Unlike the methodology presented in Section 4.2.1, we employ a different optimization methodology for the *superstructure*. The difference arises from the definition of the objective function $J$ and the type of DVs (i.e., continuous and discrete). In the single cycle optimization methodology, discussed in Section 4.2.1, all the decision variables were continuous. However, for the *superstructure* optimization, in addition to the continuous variables discussed above, we have an additional integer variable that enables switching between different process configurations. This makes the optimization a mixed integer nonlinear programming (MINLP) problem, i.e., the objective of the problem is nonlinear with both continuous and integer DVs. There are several techniques to solve such an MINLP problem, but for the sake of brevity, we do not provide a review of these methods here. We have used an off-the-shelf algorithm to optimize our *superstructure*. To this aim, we have used a single-objective derivative-free optimizer (`ga` in MATLAB R2020a) based on a methodology that mimics natural selection. Note that we could not use any off-the-shelf multiobjective optimizers, as they only take continuous DVs and not integer variables. To overcome this, we have converted the multiobjective optimization problem defined in eq 5 to a single objective problem, using a linear weighted sum method with an objective $J$ [–] defined as follows

$$J = w\left[\frac{1}{\left(Pu_{\mathrm{CO_2}}/100\right)}\right] + (1-w)\left[\frac{1}{\left(Re_{\mathrm{CO_2}}/100\right)}\right] \qquad 0 \leq w \leq 1 \tag{6}$$

where $w$ [–] is a weighting factor for the objective that corresponds to the purity maximization. Note that this method has an inherent challenge, i.e., the quality of the optimal solution depends on the choice of weights. Depending on the choice, different trade-off points

in the Pareto front can be accessed. For convex Pareto fronts, this method serves as a good proxy for multiobjective optimization. But for nonconvex Pareto fronts, the choice of the weights can potentially have an impact on the final Pareto front.[48] To overcome this challenge, we performed an initial screening of different weights to assess the accuracy of the Pareto fronts obtained from this method by comparing them with those obtained from the multiobjective optimization. Based on the outcome of this screening study, we decided to use three weighting factors, i.e., $w = [0.0,\ 0.5,\ 1.0]$ for all the optimization runs performed in this work. This choice provides good accuracy at a reasonable computational cost. Finally, note that this method, due to its nature of the formulation, does not yield equally spaced points on the Pareto front. The bounds for the continuous decision variables are provided in Section S6 in the Supporting Information. The integer variable can take one of three values, the choice of which determines which one of the configurations from the three options are chosen. The optimizer parameters for the `ga` algorithm are provided in Section S7 in the Supporting Information.

# 5 Results and Discussion

As discussed in Section 3.1, we design a *superstructure* composed of the three process configurations, based on the procedure detailed in Section 3.3. We test the performance of several adsorbents that exhibit a broad range of nonlinearity and capacity for both $CO_2$ and $H_2$ isotherms. In this section, we discuss the results obtained from a number of computational studies using the modeling and optimization framework discussed in Section 4. First, in Section 5.1, we validate the Pareto fronts obtained from the *superstructure* optimization routine, using the methodology presented in Section 4.2.2, by comparing it with the Pareto fronts obtained from independent optimizations of the constituent process configurations, with the approach presented in Section 4.2.1. Second, in Section 5.2, we formulate a simple case study, using three materials, to highlight the importance of performing an integrated

material-process optimization, i.e., "marrying" the adsorbent with the process. Finally, in Section 5.3, we highlight the relevance of performing an integrated material and process optimization. To this aim, we present: (1) the impact of feed composition on the optimal process configuration (see Section 5.3.1); (2) the impact of material isotherms on the optimal process configuration at different performance targets (see Section 5.3.2); and (3) scalability of such an approach by the addition of another process configuration to the *superstructure* (see Section 5.3.3). Note that in all the case studies shown in the subsequent sections, the goal is not to reach a specific purity/recovery target, but to highlight the importance of employing the modeling framework developed in this work for future material screening studies.

## 5.1 Validation of the *Superstructure* Optimization Routine

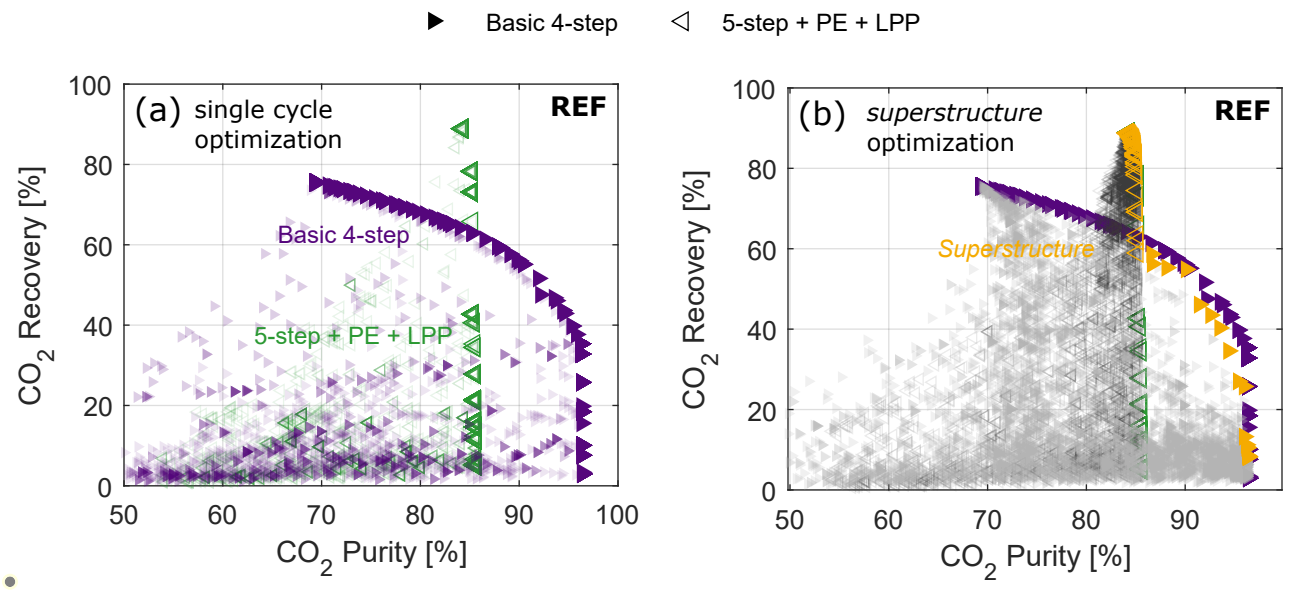


Figure 4: $CO_2$ purity/recovery Pareto fronts from the **(a)** single cycle optimization, using the methodology presented in Section 4.2.1, and **(b)** *superstructure* optimization, using the methodology presented in Section 4.2.2, for the reference material (REF). The filled right-pointing and the open left-pointing markers correspond to conditions that use the basic 4-step cycle and the 5-step cycle with PE and LPP, respectively. The transparent markers in panel (a) and the gray markers in panel (b) represent all the operating conditions explored by the optimizer and the opaque markers represent the corresponding Pareto fronts. The violet, green and gold markers correspond to the basic 4-step cycle, the 5-step cycle with PE and LPP, and the *superstructure*, respectively.

To validate the proposed optimization routine, we perform three sets of optimization runs for the reference material, namely, single cycle optimization (see Section 4.2.1) for the basic 4-step cycle and the 5-step cycle with PE and LPP, and the *superstructure* optimization (see Section 4.2.2) with these two cycles as the constituent process configurations of the *superstructure*. We aim to investigate two specific points. First, whether the *superstructure* optimization can differentiate between the two configurations. Second, whether the Pareto fronts obtained from the single cycle optimizations are comparable to the one obtained from the *superstructure*. We use the bounds of the DVs reported in Section S6 in the Supporting Information for all the material-process optimization performed here. The objective for the single cycle optimization is given by eq 5 and the corresponding objective for the superstructure optimization is given by eq 6.

The $Pu_{CO_2}/Re_{CO_2}$ Pareto fronts obtained by performing the optimization are shown in Figure 4. The transparent markers in panel (a) and the gray markers in panel (b) represent all the operating conditions explored by the optimizer and the opaque markers represent the corresponding Pareto fronts. The filled right-pointing and the open left-pointing markers correspond to conditions that use the basic 4-step cycle and the 5-step cycle with PE and LPP, respectively. We can make three observations from the Pareto fronts. First, we can see that the Pareto fronts obtained from the single cycle optimization, shown in Figure 4a, for the basic 4-step cycle (violet markers) and the 5-step cycle with PE and LPP (green markers) cross at $Re_{CO_2} \approx 60\,\%$. This can be attributed to the presence of the PE step in the 5-step cycle, which reduces $CO_2$ loss in the raffinate product due to the absence of a CoBLO step, thereby leading to higher $CO_2$ recovery. Second, we can see that the Pareto front obtained from the *superstructure* optimization (gold markers), shown in Figure 4b, agrees with the Pareto front obtained from the single cycle optimizations. We can observe minor deviations between the two cases at $Re_{CO_2} \approx 90\,\%$, which can be attributed to the stochastic nature of the optimization algorithms and the choice of optimizer parameters. Third, apart from accurately identifying the best achievable purity and recovery, the Pareto

front obtained from the *superstructure* optimization, shown in Figure 4b, also accurately identifies the choice of the process configuration to reach a given purity/recovery. In the Pareto front, at $Re_{CO_2} < 60\,\%$, the optimizer chooses the basic 4-step cycle and at $Re_{CO_2} > 60\,\%$, the optimizer chooses the 5-step cycle with PE and LPP, in line with the observations from the single cycle optimizations (see panel (a)).

Note that, here, to put our approach to a stringent test, we use two different formulations of the optimization problem (single objective vs. multiobjective) and two different optimization techniques (`patternsearch` vs. `ga`) to obtain the Pareto fronts in the two cases. Despite these differences, it is evident that the *superstructure* optimization routine used in this work is robust, in terms of predicting both the process performance and the optimal process configuration to reach the target performance. Therefore, we will use only the *superstructure* optimization routine to obtain the Pareto fronts for the different materials in the subsequent sections.

## 5.2 Marrying Materials to Processes

In this section, we apply the validated *superstructure* optimization routine described in Section 4.2.2, for three materials, namely, the reference material, material A, and material B. The latter two materials are hypothetical and are generated by changing the Sips isotherm model parameters of the reference material, as described in Section 3.2 (see Section S1 in the Supporting Information). The aim of the study presented here is to highlight that for different materials, depending on the performance targets, one can end up having different process configurations that can achieve the defined goals for the process.

The adsorption equilibrium isotherms of $CO_2$ and $H_2$ at 240 °C for the three chosen materials are shown in Figure 5a. We can see that material A (green curve) shares the same $CO_2$ isotherm with the reference material (REF, gold curve), but has a higher capacity for $H_2$ and material B (red curve) shares the same $H_2$ isotherm with the reference material (REF), but has a more nonlinear isotherm for $CO_2$. We introduce all these materials to the

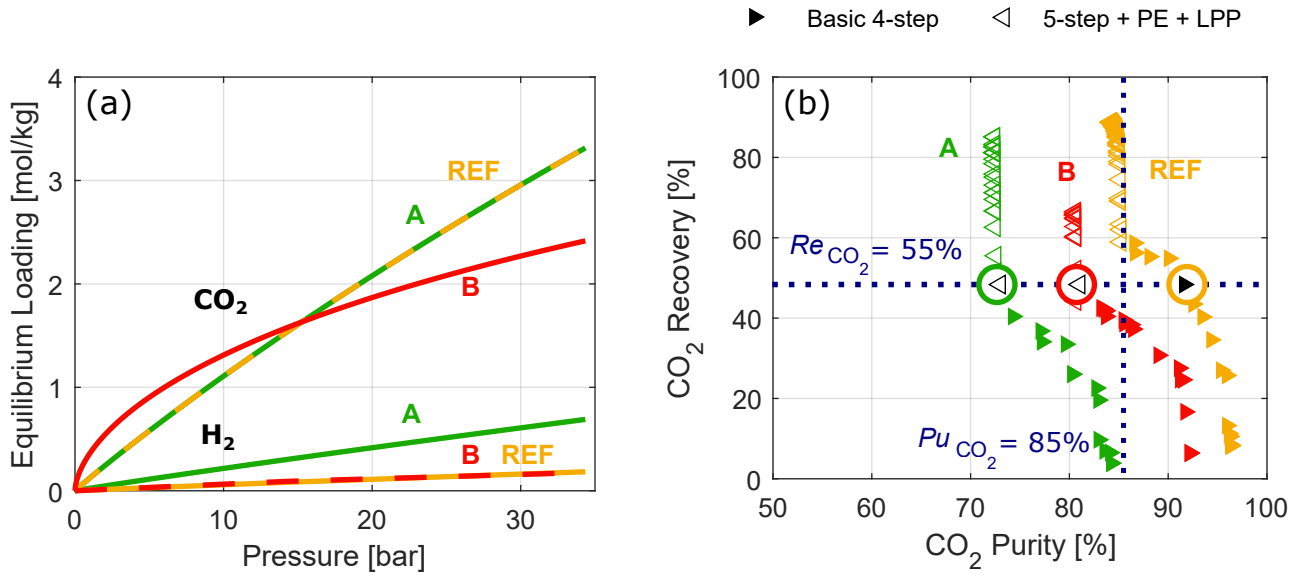


Figure 5: **(a)** Adsorption equilibrium loading obtained using the single component Sips isotherm, given by eq 1, for $CO_2$ and $H_2$ at 240 °C for the reference material (gold, REF) and the two hypothetical materials, A (green) and B (red). **(b)** The corresponding $CO_2$ purity/recovery Pareto fronts from the *superstructure* optimization, using the methodology presented in Section 4.2.2. The filled right-pointing and the open left-pointing markers correspond to conditions that use the basic 4-step cycle and the 5-step cycle with PE and LPP, respectively.

*superstructure* routine, described in Section 4.2.2, and allow it find the optimal operating conditions and the optimal process configuration to reach the best possible purity/recovery for each material. The $Pu_{CO_2}/Re_{CO_2}$ Pareto fronts obtained from these three materials are shown in Figure 5b. Note that here the superstructure is composed of two process configurations, the basic 4-step cycle (right-pointing filled triangles) and the 5-step cycle with PE and LPP (left-pointing open triangles). We use the same bounds and process operating conditions as in the previous section for all the optimization runs. From Figure 5b, we can make three observations. First, as expected, the reference material (REF), with a linear $CO_2$ isotherm and lower $H_2$ capacity performs the best and material A with the same $CO_2$ capacity and higher $H_2$ capacity as that of the reference material performs the worst.[24] Material B with a nonlinear $CO_2$ isotherm exhibits a lower $CO_2$ recovery due to its lower working capacity between the intermediate pressure $P_{INT}$ and the low pressure $P_L$. Second, all the three materials exhibit a switch in the optimal process configuration, which enables

them to truly maximize their potential. The switching $Pu_{CO_2}/Re_{CO_2}$ for the three materials are different, as they are dictated by the material isotherm. Third, for these three materials, the optimal process configuration to reach a given purity or recovery target is different. In more detail, for example at $Re_{CO_2} = 55\,\%$ (horizontal dotted line in panel (b)), one should use the basic 4-step cycle for the reference material and the 5-step cycle with PE and LPP for materials A and B to achieve the highest possible purity at this given recovery. Using the other process configuration, in either case, will lead to suboptimal performance for the given material. We can use the same argument to describe the choice of process configuration at $Pu_{CO_2} = 85\,\%$ (vertical dotted line in panel (b)). Note that using the basic 4-step cycle for the reference material at this purity target translates to a loss of around $30\,\%$ in the achievable recovery.

Based on the aforementioned observations, we can make a critical comment on the large scale material screening studies reported in the literature. Often, as described in Section 1, in most studies, the material screening is performed on a single chosen process configuration. This choice stems from prior experience studying a single reference material, for example, Zeolite 13X for postcombustion $CO_2$ capture studies. Even with the case of two process configurations, one can see from the aforementioned case study that there might be different optimal process configurations for different materials that maximize their true potential. This would mean materials that were previously considered to be "poor", in terms of their process performance, can potentially turn into promising materials simply because they have more room to explore in terms of process configurations. To summarize, based on the observations made here, we can conclude that there is a need to perform an integrated material-process optimization through a superstructure, especially for material screening purposes, that enables marrying the "right" material with the "right" process.

## 5.3 Relevance of Performing an Integrated Material and Process Optimization

### 5.3.1 Impact of Feed Composition

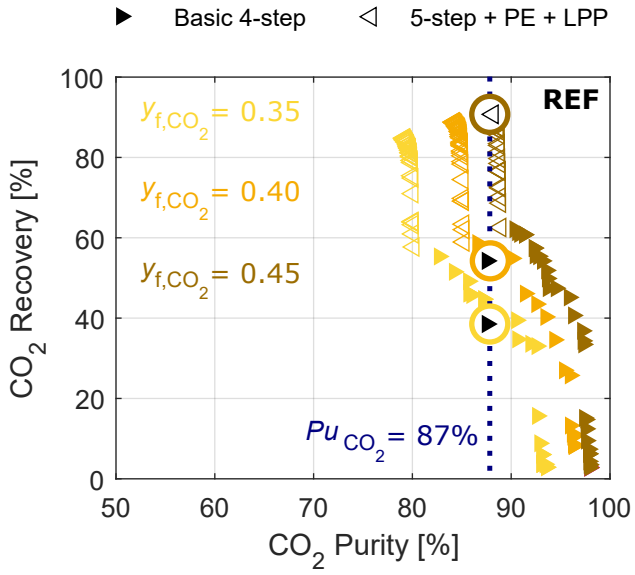


Figure 6: $CO_2$ purity/recovery Pareto fronts from the *superstructure* optimization, using the methodology presented in Section 4.2.2, at a $CO_2$ feed composition $y_{f,CO_2} = 0.35$ (yellow), $y_{f,CO_2} = 0.40$ (gold) and $y_{f,CO_2} = 0.45$ (brown) for the reference material (REF). The filled right-pointing and the open left-pointing markers correspond to conditions that use the basic 4-step cycle and the 5-step cycle with PE and LPP, respectively.

In this section, we apply the validated *superstructure* optimization routine, described in Section 4.2.2, for the reference material at different feed compositions. The aim of the study presented here is to highlight that for different feed compositions, depending on the performance targets, one can end up having different process configurations that achieve the defined goals for the process. Such an analysis is critical because in a real-world scenario one can expect fluctuations in feed compositions. Even if there are no fluctuations, one can expect differences in feed compositions depending on the source of the feed gas. For example, in the case of carbon capture applications, one can expect $CO_2$ content in the feed to be between 5 % to 40 %, depending on the source, e.g. coal, natural gas, cement, or steel.[20,49,50] However, most often studies employ a specific process configuration, optimal at a given feed

composition, for different feed composition conditions.

We perform the *superstructure* optimization for the reference material at three different $CO_2$ feed compositions, i.e., 35 %, 40 %, and 45 %. The $Pu_{CO_2}/Re_{CO_2}$ Pareto fronts obtained from these three feed compositions are shown in Figure 6. Note that here the superstructure is composed of two process configurations, the basic 4-step cycle (right-pointing filled triangles) and the 5-step cycle with PE and LPP (left-pointing open triangles). We use the same bounds and process operating conditions, except for the feed composition, as in the previous section for all the optimization runs. We can make two key observations. First, as expected, increasing the $CO_2$ feed compositions moves the Pareto front to higher values of purity and recovery due to ease of separation. Second, similar to the discussion presented in Section 5.2, all the three feed compositions exhibit a switch in the optimal process configuration. For instance, at $Pu_{CO_2} = 87\,\%$ (vertical dotted line), one should use the basic 4-step cycle for the two lowest feed compositions and the 5-step cycle with PE and LPP for the highest feed composition. The implication of such a result is amplified by observations made in other studies that highlight relaxing recovery constraints for $CO_2$ capture processes to make PSA-based separation less energy-intensive.[51] In this case, especially for the highest feed composition, allowing the process to explore different process configurations, will not just lead to a 30 % increase in the $CO_2$ recovery, but might also lead to an optimal process that has a significantly lower energy consumption due to the presence of the PE step. Even though we only present a discussion on the impact of feed composition, it is fair to assume that one can expect a similar behavior when evaluating differences in other feed conditions such as the feed pressure and temperature.

### 5.3.2 Impact of Material Isotherms

In this section, we apply the validated *superstructure* optimization routine for three more hypothetical materials, namely, materials C, D, and E. The goal of the study is to further elucidate the impact of material isotherm on the optimal process configuration. We performed

the study presented in this section to understand the influence of $CO_2$ and $H_2$ isotherms on the optimal process configuration. As has been shown in Sections 5.2 and 5.3.1, one can always encounter scenarios when the optimal process configuration to maximize the potential of a material can be different for different materials or different operating conditions.

In the first study, we introduce material C and we compare its performance with materials REF and B using the *superstructure* optimization routine. The adsorption equilibrium isotherms of $CO_2$ and $H_2$ at 240 °C for the three materials are shown in Figure 7a. We can see that material C (blue curve) shares the same $H_2$ with the other two but has a more nonlinear $CO_2$ isotherm. The $Pu_{CO_2}/Re_{CO_2}$ Pareto fronts obtained from these materials are shown in Figure 7b. The corresponding intermediate pressure $P_{INT}$ and low pressure $P_L$ as a function of the $CO_2$ recovery from the Pareto front for the three materials are illustrated in Figure 7c and Figure 7d, respectively. Note that here the superstructure is composed of two process configurations, the basic 4-step cycle (right-pointing filled triangles) and the 5-step cycle with PE and LPP (left-pointing open triangles). We use the same bounds and process operating conditions as in Section 5.2 for all the optimization runs. We can make four observations from these figures. First, the three materials exhibit different process performances that correlate well with the nonlinearity of the $CO_2$ isotherm. As seen in other studies,[13,24,49] a material with a higher nonlinearity of the $CO_2$ isotherm with the same $H_2$ isotherm as that of a material with a lower nonlinearity of the $CO_2$ isotherm, leads to poorer performance in terms of purity and recovery. Second, we can see that all the three materials exhibit a switch in the optimal process configuration. This switch happens at a much lower value of $CO_2$ purity and recovery for material C when compared to the other materials. This can be attributed to the high nonlinearity of the $CO_2$ isotherm for material C, which leads to a much lower working capacity and thereby a lower recovery. To achieve high recovery, the process has to choose a higher intermediate pressure compared to the other two materials, thereby leading to higher amount of $H_2$ in the extract product which in turn results in lower $CO_2$ purity (see Figure 7c). Third, as shown in Figure 7d, we can see that the optimizer

chooses $P_{\mathrm{L}} = 5\,\mathrm{bar}$ as the optimal low pressure, irrespective of the material to maximize $CO_2$ recovery in the extract product. Fourth, in contrast to materials REF and B, which exhibit a single switch in the optimal process configuration, we can see that material C exhibits two switches. In more detail, for material C, the basic 4-step cycle is favored at both low and high $CO_2$ purity, whereas the 5-step cycle with PE and LPP is preferred for a limited range of intermediate $CO_2$ purity. We can attribute this behavior to two factors, namely, the high nonlinearity of the $CO_2$ isotherm for material C and the bounds for the operating pressures of the process. For this material, due to the nonlinear nature of the isotherm, to maximize the $CO_2$ recovery, the optimizer uses the basic 4-step cycle and pushes the intermediate pressure $P_{\mathrm{INT}}$ close to the high pressure $P_{\mathrm{H}}$ of the process (see Figure 7c), thereby maximizing its working capacity. However, for the other two materials, the 5-step cycle with PE and LPP is sufficient to achieve maximum possible recovery for $CO_2$ despite the constant intermediate pressure (dictated by the PE step) due to a favorable shape of the $CO_2$ isotherm. If we relax the constraints on the low pressure of the process, the double switch observed for material C might disappear. Alas, in most practical applications the bounds for the process are dictated by process constraints and cannot be arbitrarily relaxed.

For the sake of clarity of the last observation, we also illustrate all the operating conditions explored by the optimizer for material C in Figure 8. Note that the right-pointing filled triangles (light gray) and the left-pointing open triangles (dark gray) correspond to the basic 4-step cycle and 5-step cycle with PE and LPP, respectively. The corresponding Pareto front is also visualized in light blue markers alongside all the operating conditions explored by the optimizer.

In the second study, we introduce two hypothetical materials, D and E and we evaluate their performance using the *superstructure* optimization routine. The adsorption equilibrium isotherms of $CO_2$ and $H_2$ at 240 °C for the two materials are shown in Figure 9a. We can see that material D (maroon curve) has a higher adsorption capacity compared to material E (green curve) for both components. The $Pu_{\mathrm{CO_2}}/Re_{\mathrm{CO_2}}$ Pareto fronts from these materials

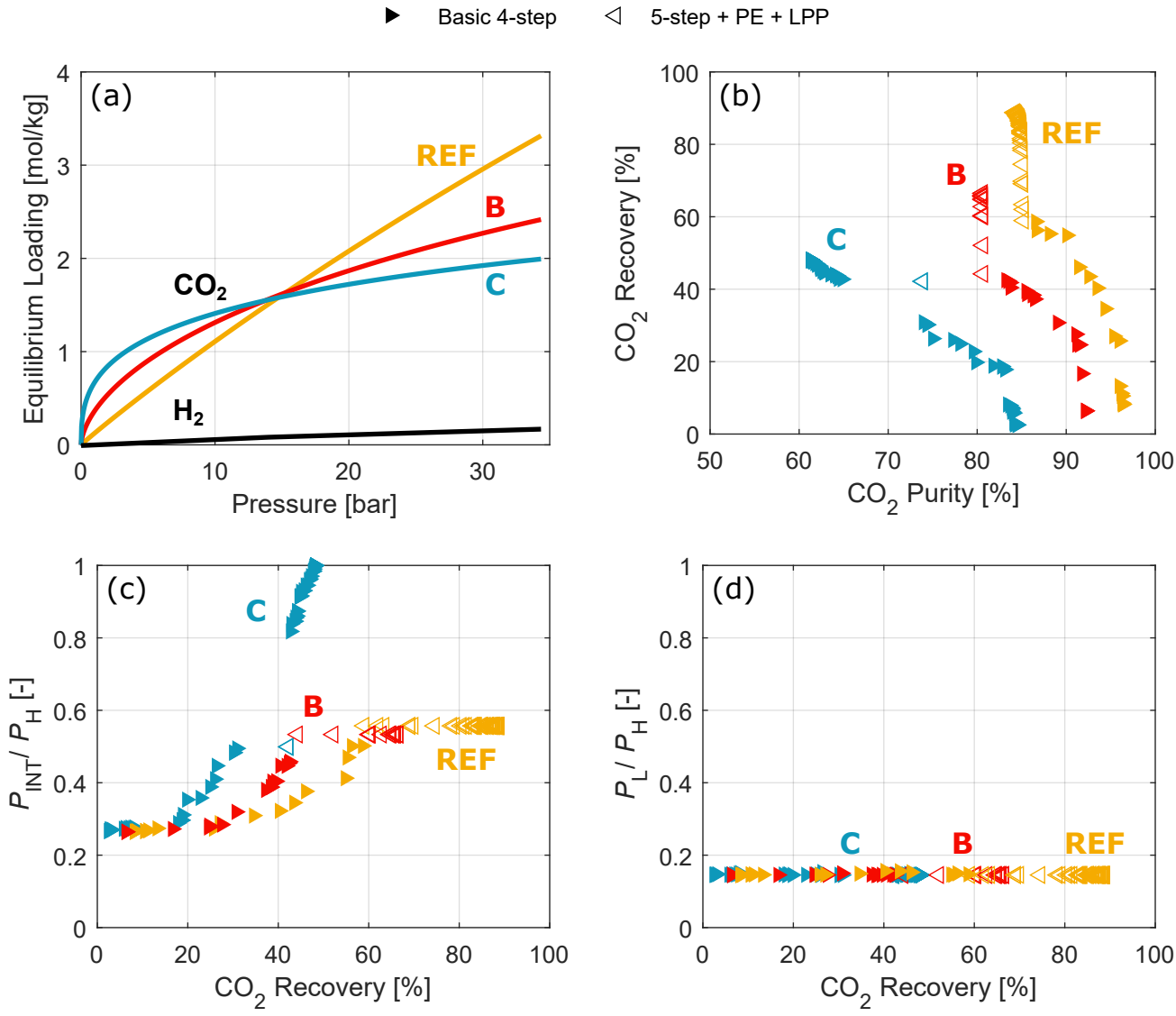


Figure 7: **(a)** Adsorption equilibrium loading obtained using the single component Sips isotherm, given by eq 1, for $CO_2$ and $H_2$ at 240 °C for the reference material (gold, REF) and the two hypothetical materials, B (red) and C (blue). The corresponding **(b)** $CO_2$ purity/recovery Pareto fronts from the *superstructure* optimization, using the methodology presented in Section 4.2.2, and the variation of **(c)** intermediate pressure $P_{\mathrm{INT}}$ and **(d)** low pressure $P_{\mathrm{L}}$ as a function of $CO_2$ recovery for the Pareto points. In panels (b) through (d), the filled right-pointing and the open left-pointing markers correspond to conditions that use the basic 4-step cycle and the 5-step cycle with PE and LPP, respectively.

are shown in Figure 9b. Note that here the superstructure is composed of two process configurations, the basic 4-step cycle (right-pointing filled triangles) and the 5-step cycle with PE and LPP (left-pointing open triangles). We use the same bounds and process

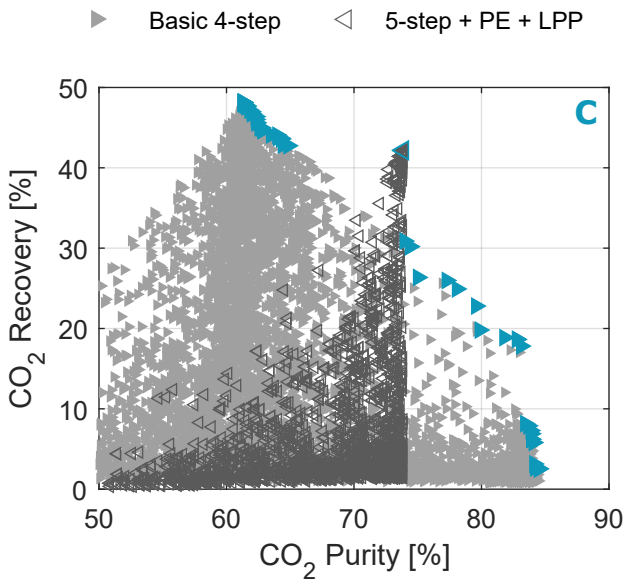


Figure 8: $CO_2$ purity/recovery Pareto front from the *superstructure* optimization, using the methodology presented in Section 4.2.2, for the hypothetical material C. The filled right-pointing and the open left-pointing markers correspond to conditions that use the basic 4-step cycle and the 5-step cycle with PE and LPP, respectively. The gray markers represent all the operating conditions explored by the optimizer and the opaque markers represent the Pareto front. Note that the axis limits here are different from the one in Figure 7.

operating conditions as in Section 5.2 for all the optimization runs. From Figure 9b, we can make two observations. First, we can see that material E exhibits a better performance than material D, due to its lower affinity toward the light component, i.e., $H_2$. Second, we can see that the two Pareto fronts overlap at $Pu_{CO_2} = 88\,\%$ to $97\,\%$. An interesting condition corresponds to $Pu_{CO_2} = 88\,\%$ and $Re_{CO_2} = 60\,\%$, highlighted by the vertical and horizontal dotted lines. In this particular scenario, material D can meet the given purity and recovery by using the basic 4-step cycle, while for material E, both the process configurations can be used. When one takes a step further and performs an energy-productivity optimization, with constraints on the purity and the recovery, it can be anticipated that for material E the 5-step cycle with PE and LPP will be possibly preferred due to the lower overall energy consumption associated with it. Therefore, applying the basic 4-step cycle to material E solely based on the findings of the optimization done for material D can potentially lead to a suboptimal and energy-intensive process. Note that performing constrained optimization,

i.e., energy-productivity optimization with constraints on purity and recovery, though not performed in this work, is a common practice in adsorption process studies.[38,46]

To conclude, the case study at different feed compositions (see Section 5.3.1) and the case study in this section with materials exhibiting differences in $CO_2$ and $H_2$ isotherm, further reinforces the relevance of performing an integrated material-process optimization using the approach presented in this work.

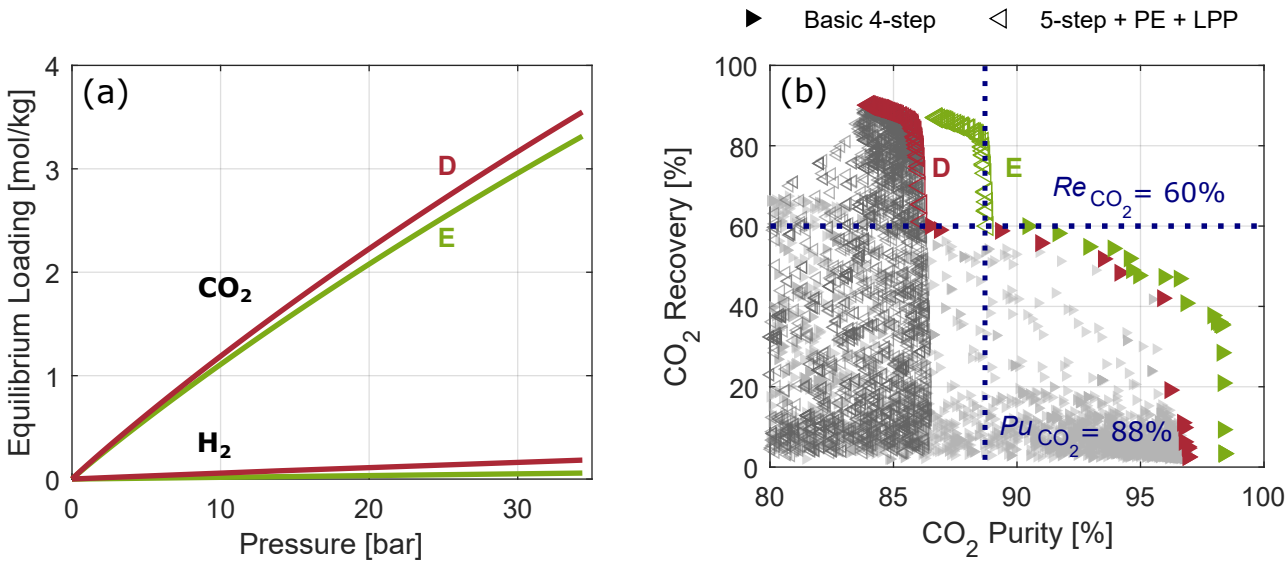


Figure 9: **(a)** Adsorption equilibrium loading obtained using the single component Sips isotherm, given by eq 1, for $CO_2$ and $H_2$ at 240 °C for two hypothetical materials, D (maroon) and E (green). **(b)** The corresponding $CO_2$ purity/recovery Pareto fronts from the *superstructure* optimization, using the methodology presented in Section 4.2.2. The filled right-pointing and the open left-pointing markers correspond to conditions that use the basic 4-step cycle and the 5-step cycle with PE and LPP, respectively. The gray markers in panel (b) represent all the operating conditions explored by the optimizer for material D and the opaque markers represent the Pareto fronts for both the materials.

### 5.3.3 Scalability of the *Superstructure*

We have restricted ourselves to two process configurations in the preceding sections and we have shown the relevance of incorporating a *superstructure*-based optimization approach. However, for the method to evolve toward a real superstructure that incorporates all possible process configurations, one should show that the modeling approach can be scaled without

losing out on the accuracy of predicting process performance. Therefore, we have introduced a third process configuration, i.e., a 4-step cycle with LPP shown in Figure 3, into the superstructure in addition to the other two process configurations. Similar to the discussion presented in Section 5.1, we compare the $Pu_{CO_2}/Re_{CO_2}$ Pareto front for the reference material obtained from the single cycle optimization, using the methodology described in Section 4.2.1, for the three process configurations with the Pareto front obtained from the *superstructure*, using the methodology described in Section 4.2.2.

The $Pu_{CO_2}/Re_{CO_2}$ Pareto fronts obtained by performing the optimization are shown in Figure 10. The transparent markers in panel (a) and the gray markers in panel (b) represent all the operating conditions explored by the optimizer and the opaque markers represent the corresponding Pareto fronts. The filled right-pointing, the open left-pointing, and the filled upward-pointing markers correspond to conditions that use the basic 4-step cycle, the 5-step cycle with PE and LPP, and the 4-step cycle with LPP, respectively. We use the same bounds and process operating conditions as in Section 5.1 for all the optimization runs. We can make three observations from the Pareto fronts. First, based on the Pareto fronts obtained from the single cycle optimization, shown in Figure 10a, we can see that the performance of the 4-step cycle with LPP (coral markers) is better than the other two process configurations. This can be attributed to the introduction of the LPP step in addition to a CoBLO step. The latter enables the optimizer to freely explore different $P_{\text{INT}}$, which is not possible with the PE step. Second, the Pareto front obtained from the *superstructure* optimization (gold markers), shown in Figure 10b, agrees with the Pareto fronts obtained from the single cycle optimization. Finally, unlike the cases discussed in the previous sections, there is no switch between different process configurations. In essence, the optimizer, after thoroughly exploring all the three process configurations (shown using markers in shades of gray), identifies the 4-step cycle with LPP to be the optimal configuration irrespective of the target purity/recovery values. Depending on the material being tested, this observation on the optimal process configuration may or may not hold. Note that we have used the

framework as is without any modification to the optimization framework.

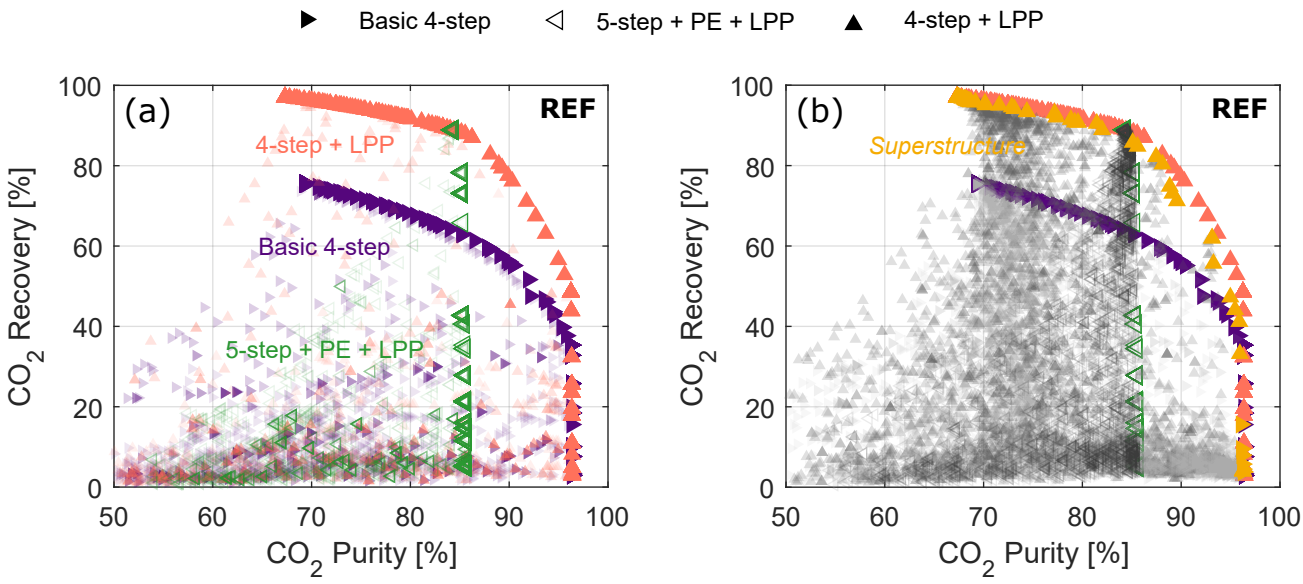


Figure 10: $CO_2$ purity/recovery Pareto fronts from the **(a)** single cycle optimization, using the methodology presented in Section 4.2.1, and **(b)** *superstructure* optimization, using the methodology presented in Section 4.2.2, for the reference material (REF). The filled right-pointing, the open left-pointing and the filled upward-pointing markers correspond to conditions that use the basic 4-step cycle, the 5-step cycle with PE and LPP, and the 4-step cycle with LPP, respectively. The transparent markers in panel (a) and the gray markers in panel (b) represent all the operating conditions explored by the optimizer and the opaque markers represent the corresponding Pareto fronts. The violet, green, coral, and gold markers correspond to the basic 4-step cycle, the 5-step cycle with PE and LPP, the 4-step cycle with LPP, and the *superstructure*, respectively.

To summarize, based on these results, we can conclude that the computational framework developed in this work shows great promise in scaling up the *superstructure* to incorporate more process configurations without losing out on the accuracy. However, an additional advantage of performing a *superstructure* optimization, that has not been discussed till now, is the time benefit obtained by optimizing multiple process configurations in one go. To highlight this additional benefit, we compare the computational time of the single cycle optimizations for the three process configurations with the computational time of the *superstructure* with both two and three process configurations. To facilitate a fair comparison between the single cycle optimization and the *superstructure* optimization, we reevaluate the optimal process performance of the constituent configurations using the approach used

to optimize the *superstructure*, i.e., with the single objective optimizer (see Section 4.2.2) instead of the multiobjective optimizer (see Section 4.2.1), but without the integer variable to choose the process configuration. In all the optimization runs, the computational budget, i.e., the total number of operating conditions explored by the optimizer, is fixed ($\approx 11\,000$ operating conditions).

The single-core computational time taken to obtain the $Pu_{CO_2}/Re_{CO_2}$ Pareto fronts from the single cycle optimization and the *superstructure* optimization is shown in Figure 11. Note that the Pareto fronts obtained from the single objective and multiobjective optimization runs for all the three process configurations are similar and these are visualized in Section S8 in the Supporting Information. We can make three key observations. First, for the single cycle optimization, depending on the process configuration, the time taken to obtain the Pareto front is different. This can be attributed to the increased computational time required to solve more complex process configurations (with more steps and complex column dynamics), for example, the 5-step cycle with PE and LPP (green bar). Second, due to the fixed computational budget for the optimization, the time for optimizing more than one process configuration using the single cycle optimization scales proportionally to the number of evaluated process configurations. This effect is shown in Figure 11 using the stacked bars for the cases of two and three cycles. Note that this would be the traditional optimization approach through which the performance of a material is evaluated independently in different process configurations. Finally, for the *superstructure*, the overall time taken for the optimization (gold bars) is the same irrespective of the number of constituent process configurations. Note that the overall time taken for the two *superstructure* optimization runs (gold bars) is similar and it is comparable to the time taken to optimize one process configuration with a single cycle optimization approach. This is expected as for a given computational budget, in the cases discussed here, the superstructure manages to explore either two or three process configurations in a single optimization run.

To conclude, based on the outcome presented here, it should be evident that the *su-*

*perstructure* approach has two main advantages. First, it guarantees to find the optimal process configuration that leads to the optimal performance for a given material. Second, and most importantly, it also shows promise in evaluating bigger superstructures with more constituent process configurations at a fraction of computational cost when compared to traditional material and process configuration screening approaches.

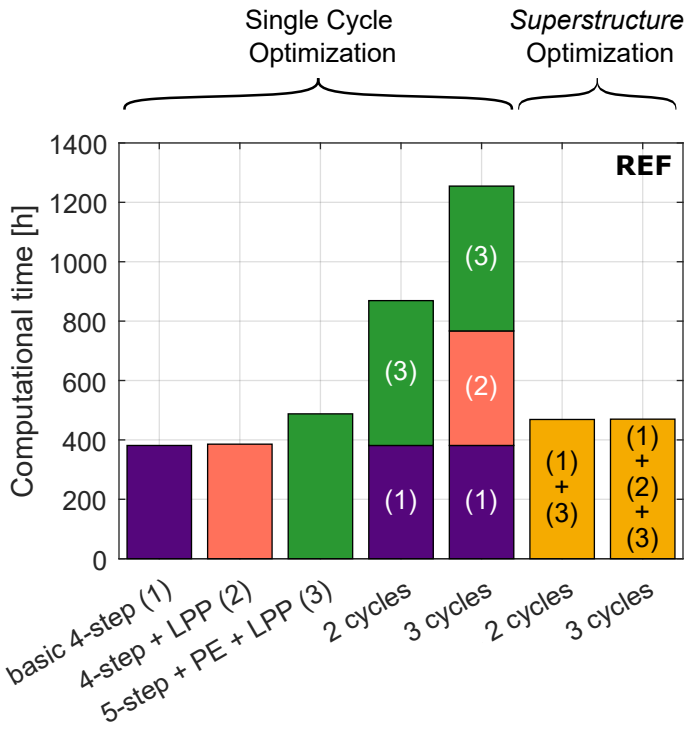


Figure 11: Single-core computational time taken to obtain the $CO_2$ purity/recovery Pareto fronts from the **(a)** single cycle optimization (the first five bars), using the methodology presented in Section 4.2.1, and **(b)** *superstructure* optimization (the last two bars), using the methodology presented in Section 4.2.2, for the reference material (REF). Note that for the two cycle and three cycle cases with the single cycle optimization, the computational time is the sum of the time taken to perform the individual cycle optimizations. The numbers in parenthesis within the bars indicate the process configurations used in the respective optimization run.

# 6 Concluding Remarks

## 6.1 Key outcomes

The work presented here builds on process-based screening of materials for adsorptive gas separation applications. We present the first superstructure inspired approach to identify the "best" material-process configuration combination for a pressure swing adsorption process. To this aim, we have developed a computational framework composed of two tools: first, we have developed a process model that can simulate a *superstructure* composed of three process configurations, and second, a process optimization routine that can optimize the entire *superstructure* to obtain both the optimal process configuration and the corresponding operating conditions. We validated and employed the computational framework on several materials to highlight the importance and relevance of the proposed approach. We can summarize the key outcomes from this work as follows:

- one should employ an integrated material-process optimization approach to truly maximize the potential of any given adsorbent used in a given gas separation application.
- one should employ an integrated material-process optimization approach to evaluate the performance of a material at different feed conditions, like the composition, pressure, and temperature.
- one should employ an integrated material-process optimization approach to conduct both purity/recovery and energy/productivity optimization to obtain a more conclusive performance of a material.
- one should not generalize observations regarding the best process configuration by evaluating the performance of a single material and subsequently extrapolating the observations to every other material. As has been long proposed, each material should be "married" to a process(es).

To conclude, we have shown through several case studies the robustness, relevance, scalability, and computational cost advantages of performing a *superstructure* optimization to optimize the performance of materials and process configurations in an integrated fashion. The key outcomes from this work and the ease with which the methodology proposed here can be extended to other systems will certainly pave the way for many new avenues in material and process screening.

## 6.2 Key Limitations and Way Forward

We acknowledge that there are a few key limitations of the work presented here. These limitations form the basis for our future work. First, the *superstructure* presented in this work is certainly not an all-encompassing cycle. However, due to reasons mentioned throughout this article, we have resorted only to three process configurations to highlight the benefits of using the approach proposed in this work. To tackle this, in our future work, we aim to redesign our superstructure with the process steps as the building block, rather than process configurations. Second, we have not put the approach to the test for other optimization problems, e.g. minimization of energy consumption and maximization of productivity of the process. An extension of this study to look into the energy consumption and productivity of the process with a true superstructure might have implications on previously reported studies that address the costing aspects of PSA-based $CO_2$ capture processes.[20,50,52] Finally, the computational time for the *superstructure* optimization despite being lower than the single cycle optimization is still significantly high, which will make screening of a large database of materials a time-consuming task. To tackle this, in our future work, we aim to exploit some of the recent advances in machine learning techniques for process optimization[26,27] to optimize the superstructure.

# Acknowledgement

A.K.R. acknowledges the assistance given by Research IT and the use of the Computational Shared Facility at The University of Manchester. S.A.H.H. and A.K.R. gratefully acknowledge the discussions with Prof. Arvind Rajendran, University of Alberta, for this work.


# Supporting Information Available

We provide the isotherm parameters for all the materials used in this work in Section S1 in the Supporting Information. We visualize the individual process configurations and their pressure profiles in Section S2 in the Supporting Information. We provide the equations and boundary conditions for the process model in Sections S3 and S4 in the Supporting Information. We provide the simulation and optimization parameters in Sections S5 and S7 in the Supporting Information. We provide the range of the decision variables used in the optimization routine in Section S6 in the Supporting Information. We illustrate the comparison of the Pareto fronts for the three process configurations obtained from a single objective and a multiobjective optimization routine in Section S8 in the Supporting Information. We provide the data associated with the simulations and the Pareto fronts for all the materials and the conditions explored in this work in a compressed file.

# References


(1) Das, N. K.; Chaudhuri, H.; Bhandari, R. K.; Ghose, D.; Sen, P.; Sinha, B. Purification of helium from natural gas by pressure swing adsorption. *Curr. Sci.* **2008**, 1684–1687.

(2) Hosseinzadeh Hejazi, S. A.; Estupiñan Perez, L.; Maruyama, R. T.; Rajendran, A.; Kuznicki, S. M. Breakthrough dynamics of nitrogen, oxygen, and argon on silver exchanged titanosilicates (Ag-ETS-10). *Adsorption* **2021**, *27*, 191–203.

(3) Zhao, R.; Zhao, L.; Deng, S.; Song, C.; He, J.; Shao, Y.; Li, S. A comparative study on $CO_2$ capture performance of vacuum-pressure swing adsorption and pressure-temperature swing adsorption based on carbon pump cycle. *Energy* **2017**, *137*, 495–509.

(4) Pullumbi, P.; Brandani, F.; Brandani, S. Gas separation by adsorption: technological drivers and opportunities for improvement. *Curr. Opin. Chem. Eng.* **2019**, *24*, 131–142.

(5) Ruthven, D. M. *Principles of adsorption and adsorption processes*; John Wiley & Sons, 1984.

(6) Sholl, D. S.; Lively, R. P. Seven chemical separations to change the world. *Nature* **2016**, *532*, 435.

(7) Das, S.; Heasman, P.; Ben, T.; Qiu, S. Porous organic materials: strategic design and structure–function correlation. *Chem. Rev.* **2017**, *117*, 1515–1563.

(8) Farmahini, A. H.; Krishnamurthy, S.; Friedrich, D.; Brandani, S.; Sarkisov, L. Performance-based screening of porous materials for carbon capture. *Chem. Rev.* **2021**, *121*, 10666–10741.

(9) Zhou, H.-C.; Long, J. R.; Yaghi, O. M. Introduction to Metal–Organic Frameworks. *Chem. Rev.* **2012**, *112*, 673–674.

(10) Bennett, T. D.; Coudert, F.-X.; James, S. L.; Cooper, A. I. The changing state of porous materials. *Nat. Mater.* **2021**, *20*, 1179–1187.

(11) Notaro, F.; Mullhaupt, J. T.; Leavitt, F. W.; Ackley, M. W. Adsorption process and system using multilayer adsorbent beds. 1997; US Patent 5,674,311.

(12) Ackley, M. W.; Stewart, A. B.; Henzler, G. W.; Leavitt, F. W.; Notaro, F.; Kane, M. S. PSA apparatus and process using adsorbent mixtures. 2000; US Patent 6,027,548.

(13) Rajagopalan, A. K.; Avila, A. M.; Rajendran, A. Do adsorbent screening metrics predict process performance? A process optimisation based study for post-combustion capture of $CO_2$. *Int. J. Greenh. Gas Control* **2016**, *46*, 76–85.

(14) Farmahini, A. H.; Krishnamurthy, S.; Friedrich, D.; Brandani, S.; Sarkisov, L. From crystal to adsorption column: challenges in multiscale computational screening of materials for adsorption separation processes. *Ind. Eng. Chem. Res.* **2018**, *57*, 15491–15511.

(15) Taddei, M.; Petit, C. Engineering metal–organic frameworks for adsorption-based gas separations: from process to atomic scale. *Mol. Syst. Des. Eng.* **2021**, *6*, 841–875.

(16) Maring, B. J.; Webley, P. A. A new simplified pressure/vacuum swing adsorption model for rapid adsorbent screening for $CO_2$ capture applications. *Int. J. Greenh. Gas Control* **2013**, *15*, 16–31.

(17) Joss, L.; Gazzani, M.; Hefti, M.; Marx, D.; Mazzotti, M. Temperature swing adsorption for the recovery of the heavy component: An equilibrium-based shortcut model. *Ind. Eng. Chem. Res.* **2015**, *54*, 3027–3038.

(18) Subramanian Balashankar, V.; Rajagopalan, A. K.; De Pauw, R.; Avila, A. M.; Rajendran, A. Analysis of a batch adsorber analogue for rapid screening of adsorbents for postcombustion $CO_2$ capture. *Ind. Eng. Chem. Res.* **2019**, *58*, 3314–3328.

(19) Ajenifuja, A.; Joss, L.; Jobson, M. A New Equilibrium Shortcut Temperature Swing Adsorption Model for Fast Adsorbent Screening. *Ind. Eng. Chem. Res.* **2020**, *59*, 3485–3497.

(20) Danaci, D.; Bui, M.; Mac Dowell, N.; Petit, C. Exploring the limits of adsorption-based $CO_2$ capture using MOFs with PVSA–from molecular design to process economics. *Mol. Syst. Des. Eng.* **2020**, *5*, 212–231.

(21) Casas, N.; Schell, J.; Pini, R.; Mazzotti, M. Fixed bed adsorption of $CO_2/H_2$ mixtures on activated carbon: experiments and modeling. *Adsorption* **2012**, *18*, 143–161.

(22) Khurana, M.; Farooq, S. Integrated adsorbent-process optimization for carbon capture and concentration using vacuum swing adsorption cycles. *AIChE J.* **2017**, *63*, 2987–2995.

(23) Nikolaidis, G. N.; Kikkinides, E. S.; Georgiadis, M. C. An integrated two-stage P/VSA process for postcombustion $CO_2$ capture using combinations of adsorbents Zeolite 13X and Mg-MOF-74. *Ind. Eng. Chem. Res.* **2017**, *56*, 974–988.

(24) Rajagopalan, A. K.; Rajendran, A. The effect of nitrogen adsorption on vacuum swing adsorption based post-combustion $CO_2$ capture. *Int. J. Greenh. Gas Control* **2018**, *78*, 437–447.

(25) Leperi, K. T.; Chung, Y. G.; You, F.; Snurr, R. Q. Development of a general evaluation metric for rapid screening of adsorbent materials for postcombustion $CO_2$ capture. *ACS Sustain. Chem. Eng.* **2019**, *7*, 11529–11539.

(26) Subraveti, S. G.; Li, Z.; Prasad, V.; Rajendran, A. Machine learning-based multiobjective optimization of pressure swing adsorption. *Ind. Eng. Chem. Res.* **2019**, *58*, 20412–20422.

(27) Yan, Y. et al. Harnessing the power of machine learning for carbon capture, utilisation, and storage (CCUS) – a state-of-the-art review. *Energy Environ. Sci.* **2021**, *14*, 6122–6157.

(28) Kawajiri, Y.; Biegler, L. T. Nonlinear programming superstructure for optimal dynamic operations of simulated moving bed processes. *Ind. Eng. Chem. Res.* **2006**, *45*, 8503–8513.

(29) Agarwal, A.; Biegler, L. T.; Zitney, S. E. Superstructure-based optimal synthesis of pressure swing adsorption cycles for precombustion $CO_2$ capture. *Ind. Eng. Chem. Res.* **2010**, *49*, 5066–5079.

(30) Sreedhar, B.; Kawajiri, Y. Multi-column chromatographic process development using simulated moving bed superstructure and simultaneous optimization–Model correction framework. *Chem. Eng. Sci.* **2014**, *116*, 428–441.

(31) Sircar, S. Pressure swing adsorption. *Ind. Eng. Chem. Res.* **2002**, *41*, 1389–1392.

(32) Rodrigues, A. E. Chemical engineering and environmental challenges. Cyclic adsorption/reaction technologies: Materials and process together! *J. Environ. Chem. Eng.* **2020**, *8*, 103926.

(33) Adjiman, C. S.; Schweiger, C. A.; Floudas, C. A. *Handbook of Combinatorial Optimization*; 1998; pp 1–76.

(34) Dubbeldam, D.; Calero, S.; Vlugt, T. J. iRASPA: GPU-accelerated visualization software for materials scientists. *Mol. Simul.* **2018**, *44*, 653–676.

(35) Haines, M.; Kemper, J.; Davison, J.; Gale, J.; Singh, P.; Santos, S. *Assessment of emerging $CO_2$ capture technologies and their potential to reduce costs*; TR 4, 2014.

(36) Subraveti, S. G.; Pai, K. N.; Rajagopalan, A. K.; Wilkins, N. S.; Rajendran, A.; Jayaraman, A.; Alptekin, G. Cycle design and optimization of pressure swing adsorption cycles for pre-combustion $CO_2$ capture. *Appl. Energy* **2019**, *254*, 113624.

(37) Dietz, S. D.; Alptekin, G.; Jayaraman, A. High capacity carbon dioxide sorbent. 2015; US Patent 9,120,079.

(38) Haghpanah, R.; Nilam, R.; Rajendran, A.; Farooq, S.; Karimi, I. A. Cycle synthesis and optimization of a VSA process for postcombustion $CO_2$ capture. *AIChE J.* **2013**, *59*, 4735–4748.

(39) Haghpanah, R.; Majumder, A.; Nilam, R.; Rajendran, A.; Farooq, S.; Karimi, I. A.; Amanullah, M. Multiobjective Optimization of a Four-Step Adsorption Process for Postcombustion $CO_2$ Capture Via Finite Volume Simulation. *Ind. Eng. Chem. Res.* **2013**, *52*, 4249–4265.

(40) LeVeque, R. J. *Finite Volume Methods for Hyperbolic Problems*; Cambridge Texts in Applied Mathematics; Cambridge University Press: Cambridge, UK, 2002; Vol. 31.

(41) Krishnamurthy, S.; Rao, V. R.; Guntuka, S.; Sharratt, P.; Haghpanah, R.; Rajendran, A.; Amanullah, M.; Karimi, I. A.; Farooq, S. $CO_2$ capture from dry flue gas by vacuum swing adsorption: A pilot plant study. *AIChE J.* **2014**, *60*, 1830–1842.

(42) Hosseinzadeh Hejazi, S. A.; Rajendran, A.; Sawada, J. A.; Kuznicki, S. M. Dynamic column breakthrough and process studies of high-purity oxygen production using silver-exchanged titanosilicates. *Ind. Eng. Chem. Res.* **2016**, *55*, 5993–6005.

(43) Hosseinzadeh Hejazi, S. A.; Estupiñan Perez, L.; Pai, K. N.; Rajendran, A.; Kuznicki, S. M. Single-and dual-stage high-purity oxygen production using silver-exchanged titanosilicates (Ag-ETS-10). *Ind. Eng. Chem. Res.* **2018**, *57*, 8997–9008.

(44) Perez, L. E.; Sarkar, P.; Rajendran, A. Experimental validation of multi-objective optimization techniques for design of vacuum swing adsorption processes. *Sep. Purif. Technol.* **2019**, *224*, 553–563.

(45) Pini, R.; Joss, L.; Hosseinzadeh Hejazi, S. A. Quantitative imaging of gas adsorption equilibrium and dynamics by X-ray computed tomography. *Adsorption* **2021**, *27*, 801–818.

(46) Hosseinzadeh Hejazi, S. A.; Estupiñan Perez, L.; Rajendran, A.; Kuznicki, S. Cycle development and process optimization of high-purity oxygen production using silver-exchanged titanosilicates. *Ind. Eng. Chem. Res.* **2017**, *56*, 5679–5691.

(47) Capra, F.; Gazzani, M.; Joss, L.; Mazzotti, M.; Martelli, E. MO-MCS, a Derivative-Free Algorithm for the Multiobjective Optimization of Adsorption Processes. *Ind. Eng. Chem. Res.* **2018**, *57*, 9977–9993.

(48) Yang, X. S. *Nature-Inspired Optim. Algorithms*; Elsevier, 2014; pp 1–263.

(49) Pai, K. N.; Prasad, V.; Rajendran, A. Practically Achievable Process Performance Limits for Pressure-Vacuum Swing Adsorption-Based Postcombustion $CO_2$ Capture. *ACS Sustain. Chem. Eng.* **2021**, *9*, 3838–3849.

(50) Subraveti, S. G.; Roussanaly, S.; Anantharaman, R.; Riboldi, L.; Rajendran, A. How much can novel solid sorbents reduce the cost of post-combustion $CO_2$ capture? A techno-economic investigation on the cost limits of pressure–vacuum swing adsorption. *Appl. Energy* **2022**, *306*, 117955.

(51) Maruyama, R. T.; Pai, K. N.; Subraveti, S. G.; Rajendran, A. Improving the performance of vacuum swing adsorption based $CO_2$ capture under reduced recovery requirements. *Int. J. Greenh. Gas Control* **2020**, *93*, 102902.

(52) Subraveti, S. G.; Roussanaly, S.; Anantharaman, R.; Riboldi, L.; Rajendran, A. Techno-economic assessment of optimised vacuum swing adsorption for post-combustion $CO_2$ capture from steam-methane reformer flue gas. *Sep. Purif. Technol.* **2021**, *256*, 117832.

# For Table of Contents Use Only

**Title:** Marrying Materials and Processes: A Superstructure Inspired Optimization Approach For Pressure Swing Adsorption Processes for Carbon Dioxide Capture

**Authors:** Amir Mohammad Elahi, Sayed Alireza Hosseinzadeh Hejazi, Ashwin Kumar Rajagopalan

**Graphical TOC Entry:**